



MXene//MnO₂ Asymmetric Supercapacitors with High Voltages and High Energy Densities

Wei Zheng,^[a] Joseph Halim,^[a] Li Yang,^[a, b] Hussein O. Badr,^[c] ZhengMing Sun,^[b] Per O. Å. Persson,^[a] Johanna Rosen,^{*[a]} and Michel W. Barsoum^{*[a, c]}

Aqueous asymmetric supercapacitors (AASCs) can have high voltages and high energy densities. However, the rational design of AASCs with proper negative and positive electrodes remains a challenge. Herein, we report on an AASC using Mo_{1.33}CT_z MXene films as the negative electrode, and tetramethylammonium cation intercalated birnessite (TMA⁺-MnO₂) films as the positive electrode in a 21 mol kg⁻¹ lithium bis(trifluoromethanesulphonyl)imide (LiTFSI) electrolyte. Benefiting from a high, stable voltage of 2.5 V, an energy density of 86.5 Wh L⁻¹ at 2 mV s⁻¹ and a power density of 10.3 kW L⁻¹ at

1 V s⁻¹ were achieved. The cells also exhibit excellent cycling stability (> 98% after 1,0000 cycles at 100 mV s⁻¹) and a 51.1% voltage retention after 10 h. This good performance is attributed to the high stable potential window and high volumetric capacitances of both Mo_{1.33}CT_z and TMA⁺-MnO₂ electrodes in highly concentrated electrolytes. This work provides a roadmap for developing high performance AASCs with high voltages and high energy/power densities, with relatively slow self-discharge rates.

Introduction

How to increase supercapacitors' (SCs) energy densities, *E*, without sacrificing power density or cycling life together with slow self-discharge, SD, rates, remains a challenge. Because *E* = 1/2 *C_s**U*², increasing *E* by extending the cell's voltage (*U*) is a more efficient method to increase their specific capacitance (*C_s*), since the *E* is proportional to the square of *U*.^[1] Although non-aqueous electrolytes are employed to extend the cell voltage currently, the preferred ones are toxic, flammable, expensive and possess low ion diffusion rates that may limit their range of applications.^[2]

Because aqueous electrolytes are safer, cheaper, greener and faster charging they have attracted great attention for use in high performance SCs. Their Achille's heel, however, is their narrow electrochemical stability window (ESW) resulting from

water splitting reactions.^[3] This is especially true if the SCs are symmetric. To solve this problem, researchers design aqueous asymmetric supercapacitors (AASCs) that take full advantage of their different operation potential windows of the negative and positive electrodes, breaking through the limitation of water splitting voltages (< 1.23 V) resulting in cell voltages > 1.4 V. Consequently, considerable work has been focused on AASCs assembled with advanced materials with large operation potential windows in aqueous electrolytes.^[4]

MXenes are a group of two dimensional (2D) layered materials, with a general formula of M_{n+1}X_nT_z or M_{1.33}CT_z, in which M is early transitional metal such as Ti, Mo, V, Nb, et al., X is carbon or/and nitrogen, *n* is 1–4, and T_z represents surface functional groups such as –F, –OH, –O, –Cl, among others.^[5] MXene with the general formula M_{1.33}CT_z were first reported on in 2017.^[6] These MXenes are derived from in-plane ordered quaternary 211 MAX phases with a formula of (M'_{1.33}M''_{0.66})AlC. After etching, both the Al layers and the minority transition metal, M'', are etched, leaving behind 2D sheets with in-plane ordered divacancies.

By now MXenes are well recognized as performing well as negative electrodes in AASCs,^[5a–c,7] because of their high conductivity, excellent hydrophilicity, great tolerance to accommodate various ions and negative operation potential window in three electrode configurations (e.g., to –1.6 V vs. Ag/AgCl in 21 M KCH₃COO^[8]).

Recently, more work has focused on MXene-based free-standing films to achieve high volumetric capacitances (C_v) in SCs due to their high density and the eschewing of inactive materials, like binders, conductive agents, etc.^[9] In previous reports, sulfuric acid (H₂SO₄) has been the electrolyte of choice. Cells typically achieve high values of C_v > 300 F g⁻¹ or > 1500 F cm⁻³.^[5d,10] However, H₂SO₄ is neither safe nor green compared with neutral aqueous electrolytes. Further issues are, i) the risk

[a] W. Zheng, J. Halim, L. Yang, P. O. Å. Persson, J. Rosen, Prof. M. W. Barsoum
Department of Physics, Chemistry and Biology (IFM)
Linköping University
581 83 Linköping, Sweden
E-mail: johanna.rosen@liu.se

[b] L. Yang, Z. Sun
School of Materials Science and Engineering
Southeast University
211189 Nanjing, People's Republic of China

[c] H. O. Badr, Prof. M. W. Barsoum
Department of Materials Science and Engineering
Drexel University
19104 Pennsylvania, Philadelphia, USA
E-mail: barsoumw@drexel.edu

 Supporting information for this article is available on the WWW under
<https://doi.org/10.1002/batt.202200151>

 © 2022 The Authors. *Batteries & Supercaps* published by Wiley-VCH GmbH. This is an open access article under the terms of the Creative Commons Attribution Non-Commercial NoDerivs License, which permits use and distribution in any medium, provided the original work is properly cited, the use is non-commercial and no modifications or adaptations are made.

of cell failure due to corrosion and by-products formation because of its acidic nature; ii) low operation potential window resulting from the occurrence of hydrogen evolution reaction (HER), and probably most importantly, iii) fast SD rates.^[11] Therefore, electrolytes such as gels or “water in salts” (WiSs) are being considered. WiSs, are highly concentrated electrolytes (salt/water ratio > 1), that have generated high interest due to their stable and high ESWs (> 2 V) and slow SD rates.^[8,12]

Mn-based nanomaterials (e.g., MnO₂, Mn₃O₄, MnOOH, etc.) possess high theoretical C_s values, low oxygen evolution reaction (OER) activity, abundance, environmental friendliness and pseudocapacitive properties,^[13] rendering them excellent positive electrode candidates in AASCs, especially when coupled with WiS electrolytes.

It is thus not surprising that AASC cells constructed using MXenes and Mn-based electrodes show enhanced electrochemical performance with high voltages and high energy densities. For example, V₂NT_z(−)//Mn₃O₄(+) AASC obtained a cell voltage of 1.8 V in 3.5 M KOH with an energy density of 15.7 Wh kg⁻¹.^[14] Ti₃C₂T₂(−)//MnO₂-Ti₃C₂T₂(+) AASC in 1 M Na₂SO₄, developed a cell voltage of 2 V, an energy density of 58 Wh kg⁻¹ and excellent rate performance.^[15] The AASC comprised of Ti₃C₂T₂(−)//MnO₂-Ti₃C₂T₂(+) in 1 M Na₂SO₄ also had an cell voltage of 2 V with an energy density of 50.1 Wh kg⁻¹.^[16] Ti₃C₂T₂(−)//V-MnO₂(+) AASC can be operated within a 2.1 V voltage, with a maximum energy density of 46 Wh kg⁻¹ in 1 M Li₂SO₄.^[17]

Although not reported, the major drawback of most, if not all, of these AASCs, is the fact that their SD rates are quite rapid for most applications (e.g., from 2.6 V to 0.5 V in 48 h^[4c] or 0.6 V to 0 V in 4 h^[11]). To counter this problem, we fabricated and tested a Ti₃C₂T₂(−)//Mn₃O₄-MnOOH(+) AASC that resulted in a cell voltage of 2.3 V, and an energy density of 30 Wh kg⁻¹ in 14 M LiCl.^[18] The SD rates of this system were significantly slower than most, if not all, dilute electrolytes.

And while 2D MnO₂ free-standing film electrodes have shown potential, the complicated preparation conditions and lengthy pre-intercalation processes have limited their large-scale production/application.^[15,19] Very recently we reported on a bottom-up approach to convert Mn₃O₄ powders into crystalline Mn-based 2D birnessite nanosheets that can be readily filtered into free-standing films with excellent flexibility.^[20] Specifically, we converted 5 different non-water soluble Mn-based precursors (Mn₃O₄, Mn₂O₃, MnB, Mn₂AlB₂ and Mn₅SiB₂) into 2D birnessite crystalline flakes via simply heating the precursor powders in 25 wt.% tetramethylammonium hydroxide (TMAH) aqueous solutions at 50°C to 80°C for 2 days, respectively. This technique is inexpensive and eminently scalable, with high yields.

Herein we show that these birnessite flakes can be used as positive electrodes directly without any other treatments or additives. The synthesis process is facile and easy to scale up. When coupled with Mo_{1.33}CT_z MXene, the Mo_{1.33}CT_z(−)//TMA⁺-MnO₂(+) AASCs result in a voltage of 2.5 V in a 21 M LiTFSI electrolyte. As far as we are aware, this is the highest reported voltage for MXene-based aqueous SCs reported to date. This AASC in turn results in high energy and power densities. Another advantage of this electrolyte is its significantly slower SD rates compared to less concentrated electrolytes that result in high energy and power densities, but as noted above, also fast SD rates that greatly narrow their applicability.

Results and Discussion

Phase composition analysis and morphology characterization

The X-ray diffraction, XRD, pattern shown in Figure 1(a), is typical of Mo_{1.33}CT_z films.^[6] The high intensity of (00l) planes indicates good stacking normal to the flakes. The (002) peak at

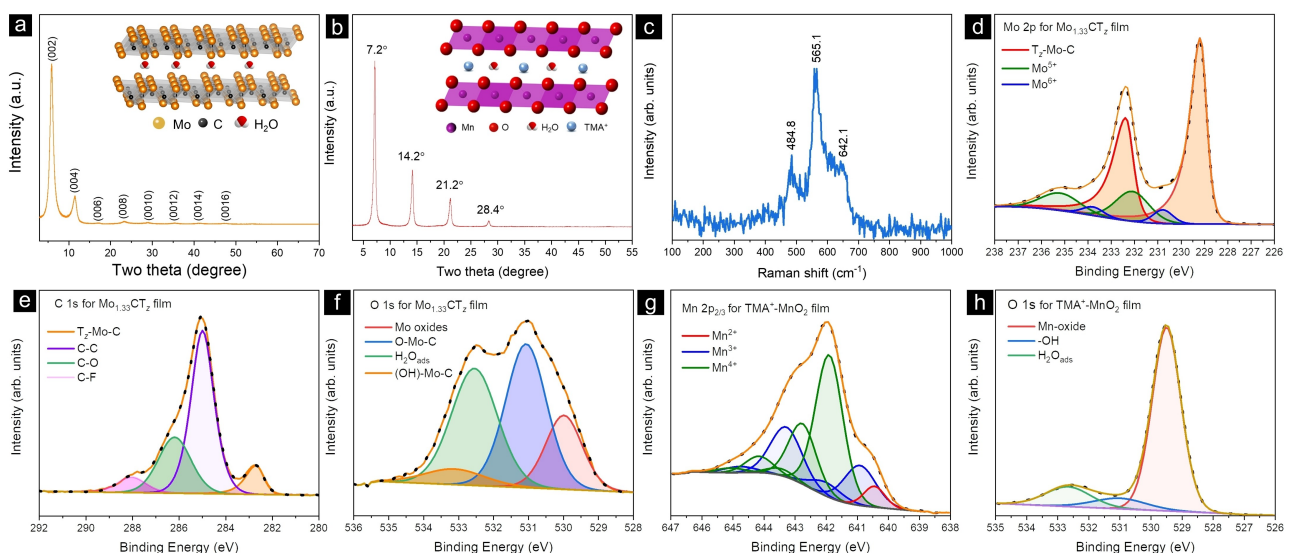


Figure 1. Characterization of electrodes. XRD patterns of a) Mo_{1.33}CT_z and b) TMA⁺-MnO₂ films; c) Raman spectra of typical TMA⁺-MnO₂ film; d) Mo 2p, e) C 1s and f) O 1s XPS spectra of Mo_{1.33}CT_z film; g) Mn 2p_{3/2} and h) O 1s of TMA⁺-MnO₂ film. Insets in a and b show atomic structures of Mo_{1.33}CT_z and TMA⁺-MnO₂, respectively.

2θ of 5.9° , corresponds to an interlayer distance, d , of 30.0 \AA . This large value presumably provides low resistance for ion transfer.

A typical XRD pattern of a $\text{TMA}^+ \cdot \text{MnO}_2$ film (Figure 1b) is characterized by peaks at 7.2° , 14.2° , 21.2° and 28.4° , that are assigned to (001), (002), (003) and (004) planes of MnO_2 birnessite.^[20] The (001) peak at 7.2° corresponds to d of 24.6 \AA . The presence of 4 distinct (00 ℓ) peaks is consistent with our previous work,^[20] and is a strong indicator that the sheets are quite well stacked normal to the sheets. When these films are heated in vacuum at 50°C for 12 h, the XRD patterns (Figure S1) indicate that the d -spacing shrinks to 9.7 \AA due to, presumably, the loss of water. If one assumes the thickness of a birnessite layer to be $\approx 2 \text{ \AA}$,^[20] this implies the TMA^+ cations are 7.7 \AA in diameter, which agrees with our previous work.^[21]

The Raman spectrum in Figure 1c shows the Mn–O stretching modes of birnessite, in which the 642.1 cm^{-1} and 565.1 cm^{-1} peaks correspond to the out-of-plane and in plane basal vibrations, respectively.^[22] The low frequency peaks are the deformation modes of the Mn–O–Mn bonds.^[23]

We further studied the effect of reaction time on the formation process of birnessite. After 12 h of heating, a small broad peak appears at $\sim 9.3^\circ$ (Figure S2b). The SEM images in Figure S3 evidence the presence of some nanosheets formed only after 5 h of heating. Due to their low content, they do not reflect in the XRD patterns. Not surprisingly, the nanosheets content increases as the reaction time is extended.

To shed light on the $\text{TMA}^+ \cdot \text{MnO}_2$ birnessite formation process, XRD patterns of pristine Mn_3O_4 powders and those heated for 48 h at 80°C in TMAH before and after sonication are shown in Figure S4(a). The major phase after heating remains Mn_3O_4 , while a peak at $\sim 9.3^\circ$ appears due to birnessite formation before sonication (Figure S4a and b). After 3 cycles of sonication, nanosheets wrapped on the Mn_3O_4 particles are still observed (Figure S4c), indicating the solid content in the colloid suspension could be increased if more sonication and centrifugation steps are used.

High-resolution X-ray photoelectron spectroscopy, XPS, spectra and the fitted results for the Mo 3d, C 1s, O 1s and F 1s regions for a typical $\text{Mo}_{1.33}\text{CT}_z$ film are shown and summarized in Figures 1(d–f) and Figure S5, Tables S1 and S2, respectively. Specifically, Mo 3d is fitted with three species (Figure 1d), including $\text{T}_z\text{-Mo-C}$ (229.2 , 232.4 eV),^[24] Mo^{+5} (230.8 , 233.8 eV)^[25] and Mo^{6+} (232.1 , 235.1 eV).^[25] The small amounts of Mo^{+5} and Mo^{6+} , most probably arise from surface oxidation of the films and was reported on previously.^[6] For C 1p (Figure 1e), the peaks correspond to the $\text{T}_z\text{-Mo-C}$ (282.7 eV),^[24] C–C (285.0 eV),^[26] C–O (286.2 eV)^[26] and C–F (288.0 eV)^[27] species. The O 1s peaks (Figure 1f) has been ascribed to Mo oxides (530.0 eV),^[25] O–Mo–C (531.1 eV), (OH)–Mo–C (532.5 eV) and $\text{H}_2\text{O}_{\text{ads}}$ (533.1 eV)^[24] peaks. Furthermore, the F 1s (Figure S5a), introduced during the HF etching process, has two peaks fitted, which are assigned to F–Mo–C (684.0 eV)^[24] and F–C (685.2 eV),^[27] respectively. Based on the XPS results, the chemical formula of the Mo containing flakes is $\approx \text{Mo}_{1.3}\text{CO}_{0.4}(\text{OH})_{0.3}\text{F}_{1.1} \cdot 0.05\text{H}_2\text{O}_{\text{ads}}$. Here we assume the base is one C.

The chemical composition on the surfaces of the $\text{TMA}^+ \cdot \text{MnO}_2$ film were also investigated by XPS, and the results are shown and summarized in Figures 1(g, h) and S5 and Tables S3–S7. The Mn 2p_{3/2} spectrum is fitted into Mn^{2+} (640.4 eV), Mn^{3+} (640.9 , 642.0 , 643.3 , 644.8 , 646.4 eV) and Mn^{4+} (641.9 , 642.8 , 643.5 , 644.2 , 645.1 eV),^[28] confirming some of the Mn in the birnessite is in +2 and +3 oxidation states, which is beneficial to its electrochemical performance (Figure 1g). The O 1s spectra (Figure 1h) fitted with O–Mn–O (529.5 eV),^[29] –OH (531.0 eV),^[29] and $\text{H}_2\text{O}_{\text{ads}}$ (532.6 eV).^[29a] The C 1s (Figure S5b) is fitted with C–C (248.8 eV), $\text{CH}_x\text{-N}$ (285.8 eV), C–O (286.1 eV), C=O (287.2 eV) and O=C=O (289.0 eV).^[26] Furthermore, nitrogen, N, (Figure S5c) is detected, and is assigned to N in $\text{TMA}^+ \cdot (\text{399.5 eV})$ ^[30] and weakly oxidized N (402.4 eV).^[30a,31] Based on the XPS analysis, we conclude that the chemical formula of the Mn-based flakes can be written as $\text{TMA}_{0.4} \cdot 0.7\text{MnO} \cdot 0.2\text{Mn}_3\text{O}_4 \cdot 11\text{MnO}_2 \cdot 5\text{H}_2\text{O}_{\text{ads}}$. In other words, most of the Mn cations are in their +4 state as previously concluded.^[20]

The $\text{Mo}_{1.33}\text{CT}_z$ and $\text{TMA}^+ \cdot \text{MnO}_2$ suspensions are dark grayish and brownish in color, respectively, and both show the Tyndall effect, confirming their colloidal states (Figure S6). After filtration, the resulting films are quite flexible (Figure 2a, b). Cross-sectional scanning electron microscope, SEM, images of both films exhibit densely stacked nanosheets (Figure 2c, d). The thicknesses are $3.15 \mu\text{m}$ and $2.82 \mu\text{m}$ for $\text{Mo}_{1.33}\text{CT}_z$ and $\text{TMA}^+ \cdot \text{MnO}_2$ films, corresponding to densities of ~ 3.5 and $\sim 3.9 \text{ g cm}^{-3}$, respectively. Elemental maps of Mo, C, O and F of a $\text{Mo}_{1.33}\text{CT}_z$ cross-section image (Figure S7) clearly show a homogeneous distribution of the elements. The absence of Al indicates the high quality of as-prepared $\text{Mo}_{1.33}\text{CT}_z$ films. Consistent with the XPS results, EDS of the $\text{TMA}^+ \cdot \text{MnO}_2$ films, detects only Mn, O, C and N (Figure S8).

In the transmission electron microscope, TEM, we find some $\text{Mo}_{1.33}\text{CT}_z$ flakes' lateral size exceeds a few microns, which is a prerequisite to obtaining flexible and intact films (Figure S9). A typical high-resolution STEM image of a $\text{Mo}_{1.33}\text{CT}_z$ nanosheet (Figure 2e) shows a rich concentration of vacancies and nanopores, which presumably provide plenty of active sites for ion storage.

When diluted and drop-cast on a scanning transmission electron microscope, STEM, grid, here again the $\text{TMA}^+ \cdot \text{MnO}_2$ nanosheets show typical lateral dimension at the micron scale (Figure 2f), some of which are folded onto themselves and crumpled. The presence of intercalated TMA^+ cations between the flakes that are rich in carbon on their surfaces renders it difficult to observe the lattice at high magnifications (Figure S10). The diffraction patterns in Figure 2(g), however, show their polycrystalline nature. The d -spacings of the rings (2.49 and 1.45 \AA), corresponding to the (001) and (110) planes of hexagonal birnessite, are in very good agreement with vertical XRD patterns of similar films reported previously.^[20] It is worth noting here that very few, if any papers, on birnessite made using a bottom-up approach at near ambient conditions include SAD patterns, presumably because of their low crystallinity. These patterns, in turn, suggest that our flakes are quite crystalline. The appearance of sharp spots on the SAED

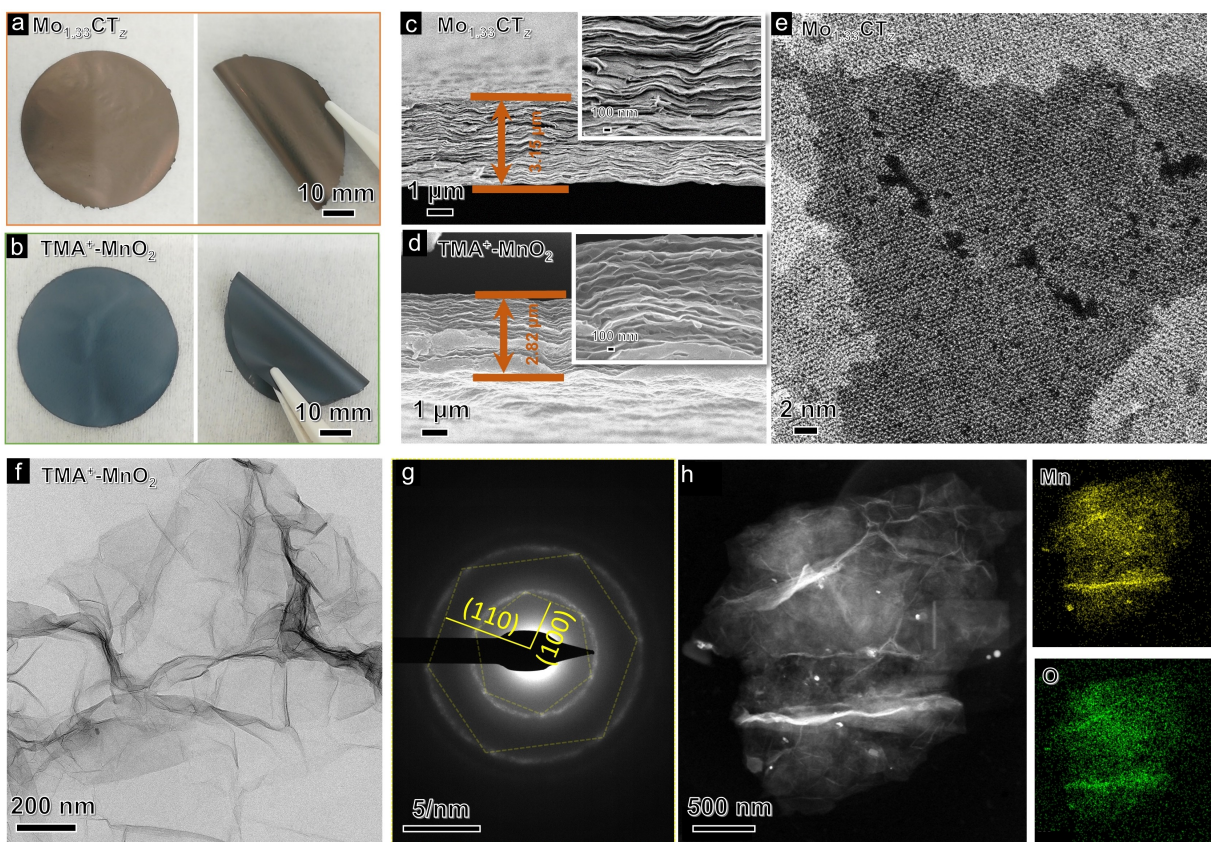


Figure 2. Pictures of a) $\text{Mo}_{1.33}\text{CT}_z$ and b) $\text{TMA}^+\text{-MnO}_2$ films. Cross-sectional SEM images of c) $\text{Mo}_{1.33}\text{CT}_z$ and d) $\text{TMA}^+\text{-MnO}_2$ films; TEM image of e) $\text{Mo}_{1.33}\text{CT}_z$ and f) $\text{TMA}^+\text{-MnO}_2$; g) typical SAED diffraction pattern of $\text{TMA}^+\text{-MnO}_2$ flakes obtained from Figure S10; h) EDS elemental maps of $\text{TMA}^+\text{-MnO}_2$ nanosheets (only Mn and O are shown), in which small nanoparticles attached to the flakes are probably unreacted Mn_3O_4 . Note hexagonal patterns in (g).

rings (Figure 2g) further confirms the crystalline nature of our flakes. The EDS elemental maps of $\text{TMA}^+\text{-MnO}_2$ nanosheets obtained from STEM (Figure 2h), clearly show the homogeneous distribution of Mn and O, which agrees well with the EDS results from SEM (Figure S8).

Electrochemical performance

The electrochemical performance of our $\text{Mo}_{1.33}\text{CT}_z$ films was measured using a 3-electrode configuration. Typical CV curves are shown in Figure 3(a). During the 1,000 pre-cycles at 20 mVs^{-1} , the shapes of the CV curves do not change, indicating a stable C_s . There is a slight increase in C_s and a near 100% coulombic efficiency, CE, (Figure 3b). At all scan rates, the CV curves are near-rectangular in shape, indicating good performance even at high rates (Figure 3c). Based on Equation (7) in Supporting Information, b is estimated to be 0.72 (Figure S11a), suggesting both capacitive and diffusive mechanisms are operational. The symmetric galvanostatic charge-discharge, GCD, curves (Figure 3d) demonstrate good reversibility, without obvious side reactions in the $-1.2 \sim 0.2 \text{ V}$ vs. Ag/AgCl potential window. Figure 3(e) plots the C_v values calculated from the CV curves as a function of scan rates. At 2 mVs^{-1} , 100 mVs^{-1} and 1000 mVs^{-1} , the C_v values are

$\sim 265.5 \text{ F cm}^{-3}$, 102.6 F cm^{-3} and $\sim 39.6 \text{ F cm}^{-3}$, respectively. These results are confirmed in Figure 3(f) as well. To summarize this section, the $\text{Mo}_{1.33}\text{CT}_z$ films exhibit good reversibility at various current densities, with near 100% CE.

The electrochemical performance of the $\text{TMA}^+\text{-MnO}_2$ films evaluated using the same 3-electrode configuration is shown in Figure 4. Compared with the $\text{Mo}_{1.33}\text{CT}_z$ films, the CV areas of the $\text{TMA}^+\text{-MnO}_2$ films gradually increase during pre-cycling (Figure 4a). More specifically, the C_v values decrease slightly initially but then keep increasing relatively rapidly up to 500 cycles, and then increase but more slowly (Figure 4b). This result is expected due to their higher density of the $\text{TMA}^+\text{-MnO}_2$ films and lower interlayer spacing, compared to the $\text{Mo}_{1.33}\text{CT}_z$ films. Here cycling opens up the interlayers, exposing new reaction sites. The fact that the $\text{Mo}_{1.33}\text{CT}_z$ films exhibited this phenomenon to a much milder degree (Figure 3b), can be ascribed to its rich concentration of vacancies and higher d values.

The CV curves of $\text{TMA}^+\text{-MnO}_2$ film from 2 to 1000 mVs^{-1} are shown in Figure 4(c). The pair of broad peaks displayed in the CV curves probably originate from changes in the Mn valence states.^[32] The b values in Figure S11(b) indicate a diffusion-controlled charge storage mechanism at low scan rates, that becomes capacitive-like at scan rates of $> 50 \text{ mVs}^{-1}$. The GCD curves in Figure 4(d) have small plateaus, in accordance with the CV curves. Based on Equations (1) and (3)

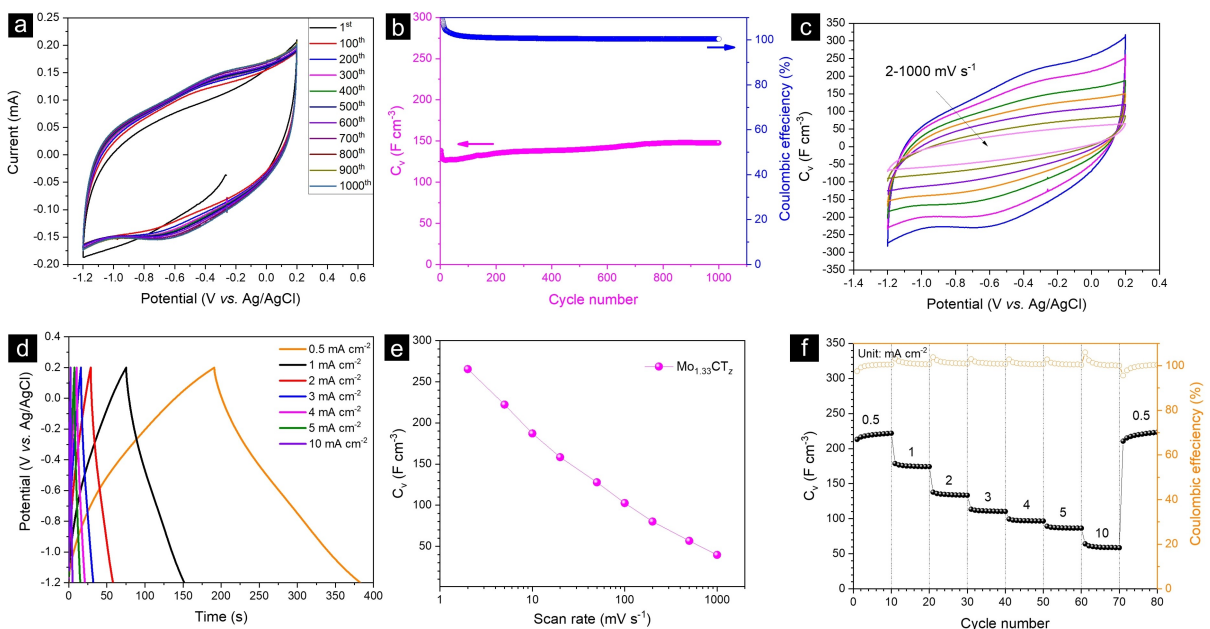


Figure 3. Electrochemical performance of $\text{Mo}_{1.33}\text{CT}_z$ film in 3-electrode configuration: a) pre-cycling at 20 mV s^{-1} for 1000 cycles; b) specific capacitance for initial 1000 cycles; c) CV curves at different scan rates from 2 to 1000 mV s^{-1} ; d) GCD curves at different current densities from 0.5 to 10 mA cm^{-2} ; e) specific capacitance as a function of scan rates; f) rate performance.

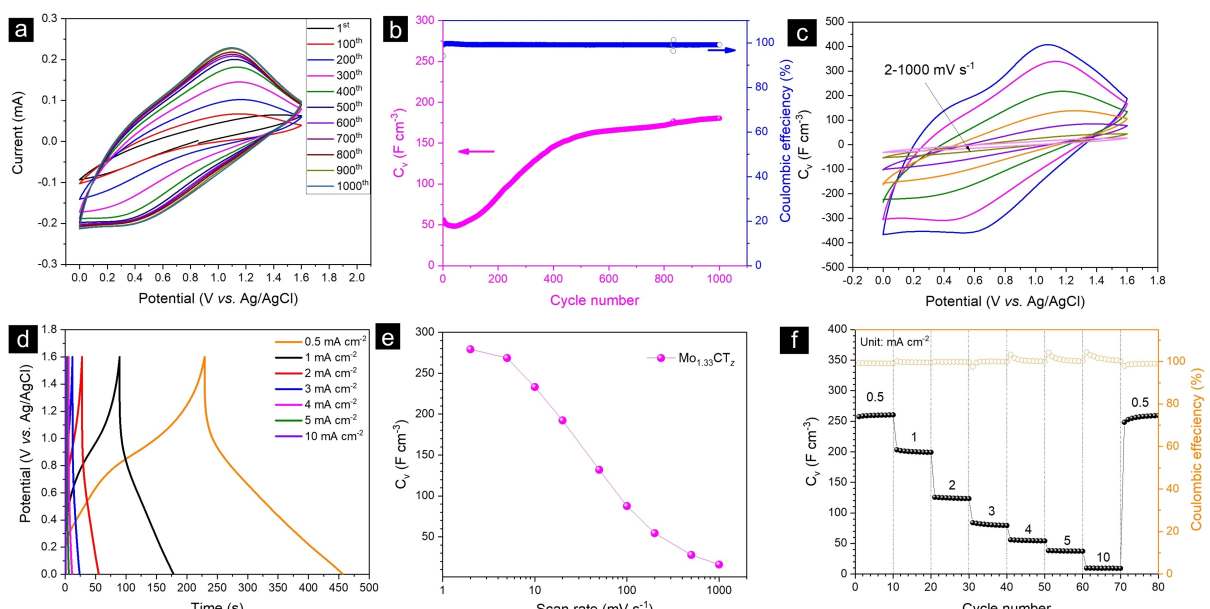


Figure 4. Electrochemical performance of $\text{TMA}^+\text{-MnO}_2$ film in 3-electrode configuration: a) pre-cycling at 20 mV s^{-1} for 1000 cycles; b) specific capacitance at the initial 1000 cycles; c) CV curves at different scan rates from 2 to 1000 mV s^{-1} ; d) GCD curves at different current densities from 0.5 to 10 mA cm^{-2} ; e) specific capacitance as a function of scan rates; f) rate performance.

in Supporting Information, the C_v value is $\sim 279.2 \text{ F cm}^{-3}$ at 2 mV s^{-1} , which is comparable to the $\text{Mo}_{1.33}\text{CT}_z$ films. Figure 4(e) shows the effect of scan rate on C_v : at 100 mV s^{-1} , 31.4% is retained which is slightly lower than the Mo-based electrode. When the scan rate is ramped up to 1000 mV s^{-1} , only $\sim 16.2 \text{ F cm}^{-3}$ are retained. This value is significantly lower than the Mo-films (Figure 3d). In summary, the $\text{TMA}^+\text{-MnO}_2$ and $\text{Mo}_{1.33}\text{CT}_z$ films have comparable C_v values at low current densities/scan

rates; at higher current densities/scan rates, the C_v values of $\text{TMA}^+\text{-MnO}_2$ film are significantly lower (Figure 4f).

Based on charge storage balance theory, $m.C.U = m_+C_+U_+$ ^[33] the mass ratio of the negative and positive electrodes should be ~ 1 , which is what is assumed here.

At 2.5 V , the voltage of our assembled cells (Figure 5a) is one of the highest values reported for MXene-based AASCs. As shown in Figure 5(a), the CV curves exhibit several peaks at low

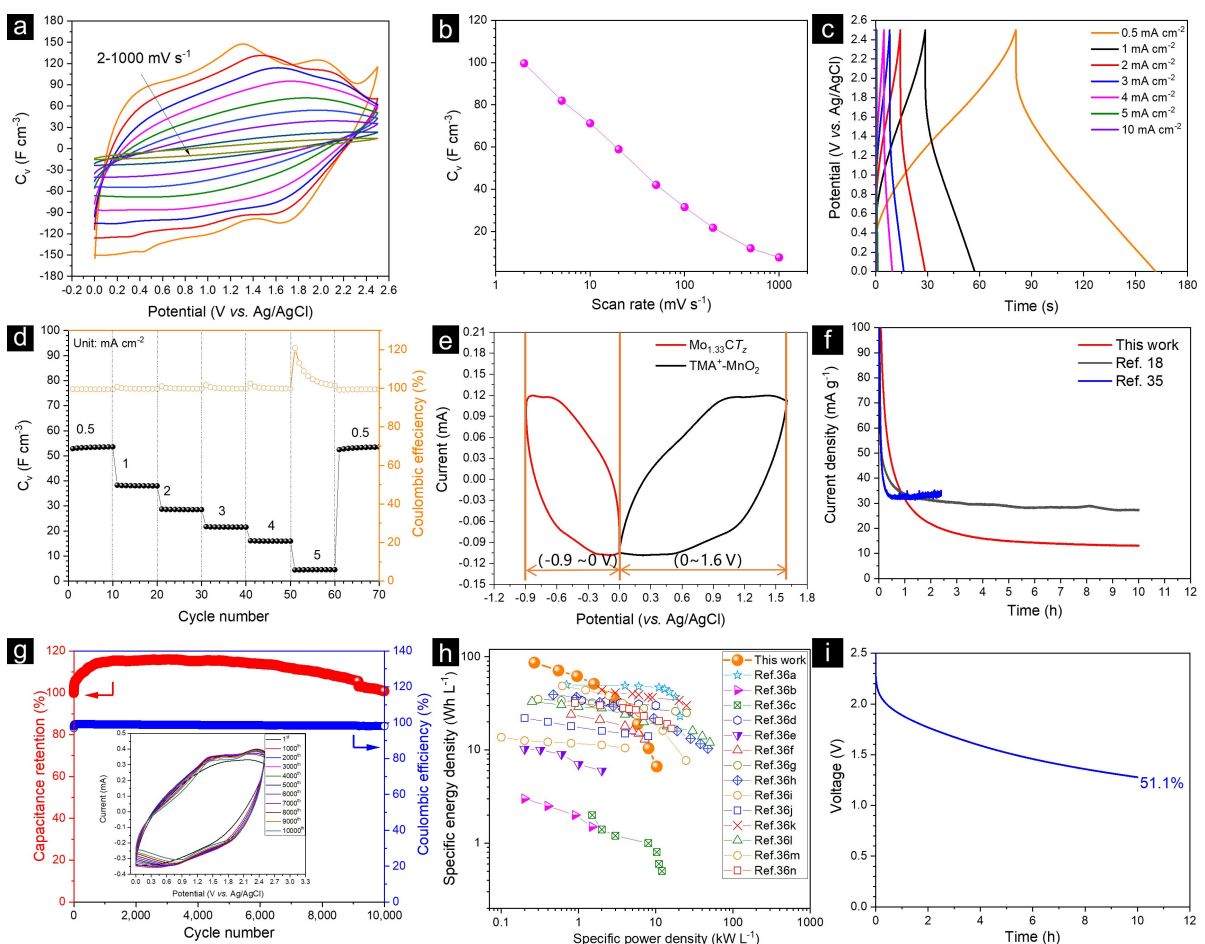


Figure 5. Electrochemical performance of the $\text{Mo}_{1.33}\text{CT}_z(-)/\text{TMA}^+\text{-MnO}_2(+)$ AASC: a) CV curves at different scan rates from 2 to 1000 mV s^{-1} ; b) specific capacitance as a function of scan rates; c) GCD curves at different current densities from 0.5 to 10 mA cm^{-2} ; d) rate performance; e) CV curves of individual electrodes at 20 mV s^{-1} ; f) time dependence of discharge current as the cell is held at 2.5 V , compared with Ref. [18,35]; g) cycling performance at 100 mV s^{-1} ; inset shows the CV curves at selected cycles from 1st to 10,000th. h) Ragone plots, compared with Ref. [36]. i) self-discharge curve. From Figure S12 the voltage retained of the $\text{Mo}_{1.33}\text{CT}_z$ electrode after 10 h was 48.5%; whereas that retained by the $\text{TMA}^+\text{-MnO}_2$ electrode was 52.4%.

scan rates, presumably due to the redox reactions of MnO_2 .^[32] Based on Equation (3) in Supporting Information, C_v is as high as 99.6 F cm^{-3} at 2 mV s^{-1} (Figure 5b). As the current density increases, C_v is reduced to 31.6 F cm^{-3} at 100 mV s^{-1} and 7.7 F cm^{-3} at 1000 mV s^{-1} . These values are quite good considering that no conductive binders are used, especially to the Mn-based electrodes. Said otherwise, it is reasonable to assume that the rate performance can be readily enhanced if conductive binders, such as CNTs or graphene, are used to prepare the electrodes.

The discharge time is almost equal to the charge time in the $0\text{--}2.5 \text{ V}$ range, indicating good reversibility (Figure 5c). The IR drop in Figure 5(c) can most probably be ascribed to the relatively low electronic conductivity of the $\text{TMA}^+\text{-MnO}_2$ composite electrode and/or the low ionic conductivity of the concentrated LiTFSI electrolyte. The effect of rate on C_v (Figure 5d) shows relatively low values at high current densities. The CE at low rates are stable ($\sim 100\%$), but become abnormal at 5 mA cm^{-2} , probably because of the sudden large current changes. This assumption is based on the CE becoming stable again after 6–7 cycles at 0.5 mA cm^{-2} .

Both the negative and positive electrodes fall to their safe potential window at 20 mV s^{-1} (Figure 5e), leading to a low leakage current of $\sim 14 \text{ mA g}^{-1}$. The actual current, not normalized by mass, is $\sim 3.9 \mu\text{A}$ after 10 h (Figure 5f). In comparison, the $\text{Ti}_3\text{C}_2\text{T}_2(-)/\text{Mn}_3\text{O}_4\text{-MnOOH}(+)$ AASC and $\text{Mo}_{1.33}\text{CT}_z/\text{Mo}_{1.33}\text{CT}_z$ SSC have leakage currents of $\sim 35 \text{ mA g}^{-1}$ and $\sim 30 \text{ mA g}^{-1}$, respectively,^[18,34] indicating a further advantage of our device. Furthermore, the cycling performance at 100 mV s^{-1} for 10,000 cycles is stable ($> 98\%$), as shown in Figure 5(g). Based on Equations (5) and (6) in Supporting Information, the highest energy density is 86.5 Wh L^{-1} (at a power density of 267.8 WL^{-1}) and the highest power density is 10.3 kW L^{-1} (at an energy density of 6.6 Wh L^{-1}), which is outstanding when compared with previously reported energy densities as shown in the Ragone plot (Figure 5h) and summarized in Table S8. It should be noted that the values taken from the literature are obtained in low concentration H_2SO_4 , LiCl or KOH electrolytes, that invariably lead to quite fast SD rates.^[11]

From a practical point of view, an energy storage device that cannot store charge for a long time has limited applic-

ability. For our cell, we show that after 10 h, the voltage drops from 2.5 V to \sim 1.3 V, corresponding to a 51.1% retention (Figure 5i). The individual SD curves for the negative and positive electrodes are shown in Figure S12. We have previously shown that the SD of MXene-based SCs is mainly due to parasitic faradaic reactions arising from impurities, especially oxygen. We also showed that concentrated electrolytes perform significantly better than say H_2SO_4 , one of the more popular electrolytes, because it resulted in quite high specific capacitances.^[11,18] We also showed that the onset of diffusion control was a function of electrolyte concentrations, with higher concentrations (e.g., 14 M LiCl or LiBr) leading to a faster onset of diffusion limited regimes.^[18] Plotting our SD results as a function of $t^{1/2}$ and $\ln t$ in Figure S13(a and b), respectively, suggests that a diffusion-controlled process sets in after $t > 900$ s, with a R^2 value of 0.9987 (Figure S13a). It should be noted that the SD performance in this work, while still reasonably fast, is significantly slower than that in low-concentrated electrolytes (Figure S14).^[11] It is hereby acknowledged that our SD rates, while at least an order of magnitude better than less concentrated electrolytes, need to be greatly improved for some applications. According to our previous work,^[11] the use of high purity LiTFSI would be an obvious path forward.

Conclusion

A new and facile, scalable, synthesis protocol is used to fabricate crystalline $TMA^+ \cdot MnO_2$ birnessite nanosheets. The obtained films have a wide potential window (0–1.6 V) in a 21 mol kg⁻¹ concentrated LiTFSI electrolyte. When coupled with a positive electrode comprised of $Mo_{1.33}CT_z$ MXene films, at 2.5 V, our device exhibits the highest voltage for a MXene-based or aqueous electrolyte-based SC. This results in AASCs with high energy/power density (86.5 Wh L⁻¹/267.8 WL⁻¹ at 2 mVs⁻¹ and 6.6 Wh L⁻¹/10.3 kW L⁻¹ at 1 Vs⁻¹). The SD rate (51.1% voltage retention after 10 h) is relatively slow compared to less concentrated electrolytes, but needs to be further enhanced for many applications.

This work provides a roadmap for further development of new electrodes and choice of electrolyte for high performance practical supercapacitors.

Acknowledgements

This work is supported by the Swedish Foundation for Strategic Research (SSF) EM16-0004. J.R. also acknowledges funding from the Knut and Alice Wallenberg (KAW) foundation for a Fellowship/Scholar grant. P.O.Å.P. also acknowledges Swedish Foundation for Strategic Research (SSF) through the Research Infrastructure Fellow program no. RIF 14–0074. We also would like to thank Dr. Justinas Palisaitis for his help with STEM measurements.

Conflict of Interest

The authors declare no conflict of interest.

Data Availability Statement

The data that support the findings of this study are available from the corresponding author upon reasonable request.

Keywords: birnessite MnO_2 • high energy density • high voltage • MXene • supercapacitors

- [1] a) L. Demarconnay, E. Raymundo-Piñero, F. Béguin, *J. Power Sources* **2011**, *196*, 580–586; b) G. Zhang, H. Yao, F. Zhang, Z. Gao, Q. Li, Y. Yang, X. Lu, *Nano Res.* **2019**, *12*, 1061–1069.
- [2] D. Chao, W. Zhou, F. Xie, C. Ye, H. Li, M. Jaroniec, S.-Z. Qiao, *Sci. Adv.* **2020**, *6*, eaba4098.
- [3] H. Kim, J. Hong, K.-Y. Park, H. Kim, S.-W. Kim, K. Kang, *Chem. Rev.* **2014**, *114*, 11788–11827.
- [4] a) T. Xiong, T. L. Tan, L. Lu, W. S. V. Lee, J. Xue, *Adv. Energy Mater.* **2018**, *8*, 1702630; b) N. Jabeen, A. Hussain, Q. Xia, S. Sun, J. Zhu, H. Xia, *Adv. Mater.* **2017**, *29*, 1700804; c) X. Wu, B. Huang, Q. Wang, Y. Wang, *J. Mater. Chem. A* **2019**, *7*, 19017–19025.
- [5] a) M. Ghidiu, M. R. Lukatskaya, M. Q. Zhao, Y. Gogotsi, M. W. Barsoum, *Nature* **2014**, *516*, 78–81; b) M. Naguib, M. Kurtoglu, V. Presser, J. Lu, J. Niu, M. Heon, L. Hultman, Y. Gogotsi, M. W. Barsoum, *Adv. Mater.* **2011**, *23*, 4248–4253; c) Y. Li, H. Shao, Z. Lin, J. Lu, L. Liu, B. Dupoyer, P. O. Å Persson, P. Eklund, L. Hultman, M. Li, K. Chen, X.-H. Zha, S. Du, P. Rozier, Z. Chai, E. Raymundo-Piñero, P.-L. Taberna, P. Simon, Q. Huang, *Nat. Mater.* **2020**, *23*, 4248–4253; d) B. Ahmed, A. E. Ghazaly, J. Rosen, *Adv. Funct. Mater.* **2020**, *30*, 2000894.
- [6] Q. Tao, M. Dahlqvist, J. Lu, S. Kota, R. Meshkian, J. Halim, J. Palisaitis, L. Hultman, M. W. Barsoum, P. O. Å Persson, J. Rosen, *Nat. Commun.* **2017**, *8*, 14949.
- [7] a) Q. Jiang, N. Kurra, M. Alhabeb, Y. Gogotsi, H. N. Alshareef, *Adv. Energy Mater.* **2018**, *8*, 1703043; b) R. Zhao, M. Wang, D. Zhao, H. Li, C. Wang, L. Yin, *ACS Energy Lett.* **2018**, *3*, 132–140; c) M. Boota, Y. Gogotsi, *Adv. Energy Mater.* **2019**, *9*, 1802917; d) A. S. Etman, J. Halim, J. Rosen, *Materials Advances* **2021**, *2*, 743–753.
- [8] H. Avireddy, B. W. Byles, D. Pinto, J. M. Delgado Galindo, J. J. Biendicho, X. Wang, C. Flox, O. Crosnier, T. Brousse, E. Pomerantseva, J. R. Morante, Y. Gogotsi, *Nano Energy* **2019**, *64*, 103961.
- [9] a) M. R. Lukatskaya, O. Mashtalir, C. E. Ren, Y. Dall'Agnese, P. Rozier, P. L. Taberna, M. Naguib, P. Simon, M. W. Barsoum, Y. Gogotsi, *Science* **2013**, *341*, 1502–1505; b) O. Mashtalir, M. Naguib, V. N. Mochalin, Y. Dall'Agnese, M. Heon, M. W. Barsoum, Y. Gogotsi, *Nat. Commun.* **2013**, *4*, 1716; c) M. Ghidiu, M. R. Lukatskaya, M.-Q. Zhao, Y. Gogotsi, M. W. Barsoum, *Nature* **2014**, *516*, 78–81; d) J. Kong, H. Yang, X. Guo, S. Yang, Z. Huang, X. Lu, Z. Bo, J. Yan, K. Cen, K. K. Ostrikov, *ACS Energy Lett.* **2020**, *5*, 2266–2274.
- [10] M. R. Lukatskaya, S. Kota, Z. Lin, M.-Q. Zhao, N. Shpigel, M. D. Levi, J. Halim, P.-L. Taberna, M. W. Barsoum, P. Simon, Y. Gogotsi, *Nat. Energy* **2017**, *2*, 17105.
- [11] W. Zheng, J. Halim, J. Rosen, M. W. Barsoum, *Adv. Energy Sustainability Res.* **3**, 2100147.
- [12] a) L. Suo, O. Borodin, T. Gao, M. Olguin, J. Ho, X. Fan, C. Luo, C. Wang, K. Xu, *Science* **2015**, *350*, 938–943; b) M. Zhang, Y. Li, Z. Shen, *J. Power Sources* **2019**, *414*, 479–485; c) Z. Song, H. Duan, D. Zhu, Y. Lv, W. Xiong, T. Cao, L. Li, M. Liu, L. Gan, *J. Mater. Chem. A* **2019**, *7*, 15801–15811; d) X. Liu, R. Mi, L. Yuan, F. Yang, Z. Fu, C. Wang, Y. Tang, *Front. Chem.* **2018**, *6*, 475.
- [13] M. Toupin, T. Brousse, D. Bélanger, *Chem. Mater.* **2004**, *16*, 3184–3190.
- [14] S. Venkateshalu, J. Cherusseri, M. Karnan, K. S. Kumar, P. Kollu, M. Sathish, J. Thomas, S. K. Jeong, A. N. Grace, *ACS Omega* **2020**, *5*, 17983–17992.
- [15] F. Zhao, W. Liu, T. Qiu, W.-B. Gong, W. Ma, Q. Li, F. Li, F. Geng, *ACS Nano* **2020**, *14*, 603–610.

- [16] Z. Bo, K. Yi, H. Yang, X. Guo, Z. Huang, Z. Zheng, J. Yan, K. Cen, K. Ostrikov, *J. Power Sources* **2021**, *492*, 229639.
- [17] J. Wu, Q. Li, C. E. Shuck, K. Maleski, H. N. Alshareef, J. Zhou, Y. Gogotsi, L. Huang, *Nano Res.* **2021**, *15*, 535–541.
- [18] W. Zheng, J. Halim, Z. Sun, J. Rosen, M. W. Barsoum, *Energy Storage Mater.* **2021**, *38*, 438–446.
- [19] Y. Omomo, T. Sasaki, L. Wang, M. Watanabe, *J. Am. Chem. Soc.* **2003**, *125*, 3568–3575.
- [20] H. O. Badr, K. Montazeri, T. El-Melegy, V. Natu, M. Carey, R. Gawas, P. Phan, Q. Qian, C. Y. Li, U. Wiedwald, M. Farle, E. Colin-Ulloa, L. V. Titova, M. Currie, T. Ouisse, M. Barbier, A. Rogalev, F. Wilhelm, M. Hans, J. M. Schneider, C. Tandoc, Y.-J. Hu, J. Snyder, M. W. Barsoum, *Matter* **2022**, <https://doi.org/10.1016/j.matt.2022.05.038>.
- [21] H. O. Badr, T. El-Melegy, M. Carey, V. Natu, M. Q. Hassig, C. Johnson, Q. Qian, C. Y. Li, K. Kushnir, E. Colin-Ulloa, L. V. Titova, J. L. Martin, R. L. Grimm, R. Pai, V. Kalra, A. Karmakar, A. Ruffino, S. Masiuk, K. Liang, M. Naguib, O. Wilson, A. Magenau, K. Montazeri, Y. Zhu, H. Cheng, T. Torita, M. Koyanagi, A. Yanagimachi, T. Ouisse, M. Barbier, F. Wilhelm, A. Rogalev, J. Björk, P. O. Å Persson, J. Rosen, Y.-J. Hu, M. W. Barsoum, *Mater. Today* **2021**, *54*, 8–17.
- [22] L. Yang, S. Cheng, J. Wang, X. Ji, Y. Jiang, M. Yao, P. Wu, M. Wang, J. Zhou, M. Liu, *Nano Energy* **2016**, *30*, 293–302.
- [23] C. M. Julien, M. Massot, C. Poinsignon, *Spectrochim. Acta Part A* **2004**, *60*, 689–700.
- [24] H. Lind, J. Halim, S. I. Simak, J. Rosen, *Phys. Rev. Mater.* **2017**, *1*, 044002.
- [25] a) F. Werfel, E. Minni, *J. Phys. C* **1983**, *16*, 6091–6100; b) K. Arata, M. Hino, *Appl. Catal.* **1990**, *59*, 197–204.
- [26] a) A. Proctor, P. M. A. Sherwood, *Surf. Interface Anal.* **1982**, *4*, 212–219; b) E. Desimoni, G. I. Casella, A. Morone, A. M. Salvi, *Surf. Interface Anal.* **1990**, *15*, 627–634; c) Y. Xie, P. M. A. Sherwood, *Chem. Mater.* **1989**, *1*, 427–432.
- [27] T. Nakajima, Y. Matsuo, B. Žemva, A. Jesih, *Carbon* **1996**, *34*, 1595–1598.
- [28] M. C. Biesinger, B. P. Payne, A. P. Grosvenor, L. W. M. Lau, A. R. Gerson, R. S. C. Smart, *Appl. Surf. Sci.* **2011**, *257*, 2717–2730.
- [29] a) H. W. Nesbitt, D. Banerjee, *Am. Mineral.* **1998**, *83*, 305–315; b) M. Kang, E. D. Park, J. M. Kim, J. E. Yie, *Appl. Catal. A* **2007**, *327*, 261–269.
- [30] a) D. A. Svintsitskiy, L. S. Kibis, D. A. Smirnov, A. N. Suboch, O. A. Stonkus, O. Y. Podyacheva, A. I. Boronin, Z. R. Ismagilov, *Appl. Surf. Sci.* **2018**, *435*, 1273–1284; b) S. Kuroki, Y. Hosaka, C. Yamauchi, M. Sonoda, Y. Nabae, M.-A. Kakimoto, S. Miyata, *J. Electrochem. Soc.* **2012**, *159*, F309–F315; c) D. Geng, S. Yang, Y. Zhang, J. Yang, J. Liu, R. Li, T.-K. Sham, X. Sun, S. Ye, S. Knights, *Appl. Surf. Sci.* **2011**, *257*, 9193–9198; d) G. He, M. Qiao, W. Li, Y. Lu, T. Zhao, R. Zou, B. Li, J. A. Darr, J. Hu, M.-M. Titirici, I. P. Parkin, *Adv. Sci.* **2017**, *4*, 1600214; e) K. N. Wood, S. T. Christensen, D. Nordlund, A. A. Dameron, C. Ngo, H. Dinh, T. Gennett, R. O’Hayre, S. Pylypenko, *Surf. Interface Anal.* **2016**, *48*, 283–292; f) J. Melke, B. Peter, A. Haberer, J. Ziegler, C. Fasel, A. Nefedov, H. Sezen, C. Wöll, H. Ehrenberg, C. Roth, *ACS Appl. Mater. Interfaces* **2016**, *8*, 82–90.
- [31] a) X. Liang, J. Zhong, Y. Shi, J. Guo, G. Huang, C. Hong, Y. Zhao, *Mater. Res. Bull.* **2015**, *61*, 252–258; b) R. Arrigo, M. E. Schuster, Z. Xie, Y. Yi, G. Wownick, L. L. Sun, K. E. Hermann, M. Friedrich, P. Kast, M. Hävecker, A. Knop-Gericke, R. Schlögl, *ACS Catal.* **2015**, *5*, 2740–2753.
- [32] a) S. Wen, J.-W. Lee, I.-H. Yeo, J. Park, S.-I. Mho, *Electrochim. Acta* **2004**, *50*, 849–855; b) L. Athouél, F. Moser, R. Dugas, O. Crosnier, D. Bélanger, T. Brousse, *J. Phys. Chem. C* **2008**, *112*, 7270–7277.
- [33] Y. Shao, M. F. El-Kady, J. Sun, Y. Li, Q. Zhang, M. Zhu, H. Wang, B. Dunn, R. B. Kaner, *Chem. Rev.* **2018**, *206*, 270–276.
- [34] Z. Wei, Z. Peigen, T. Wubian, Q. Xia, Z. Yamei, S. ZhengMing, *Mater. Chem. Phys.* **2018**, *206*, 270–276.
- [35] W. Zheng, J. Halim, P. O. Å Persson, J. Rosen, M. W. Barsoum, *Mater. Rep. Ener.* **2022**, *2*, 100078.
- [36] a) K. Li, X. Wang, S. Li, P. Urbankowski, J. Li, Y. Xu, Y. Gogotsi, *Small* **2020**, *16*, 1906851; b) H. Li, Y. Hou, F. Wang, M. R. Lohe, X. Zhuang, L. Niu, X. Feng, *Adv. Energy Mater.* **2017**, *7*, 1601847; c) A. VahidMohammadi, M. Mojtabavi, N. M. Caffrey, M. Wanunu, M. Beidaghi, *Adv. Mater.* **2019**, *31*, 1806931; d) L. Zhang, D. Han, Y. Tao, C. Cui, Y. Deng, X. Dong, W. Lv, Z. Lin, S. Wu, Z. Weng, Q.-H. Yang, *J. Mater. Chem. A* **2020**, *8*, 461–469; e) A. M. Navarro-Suárez, K. L. Van Aken, T. Mathis, T. Makaryan, J. Yan, J. Carretero-González, T. Rojo, Y. Gogotsi, *Electrochim. Acta* **2018**, *259*, 752–761; f) L. Li, N. Zhang, M. Zhang, X. Zhang, Z. Zhang, *Dalton Trans.* **2019**, *48*, 1747–1756; g) L. Qin, Q. Tao, A. El Ghazaly, J. Fernandez-Rodriguez, P. O. Å Persson, J. Rosen, F. Zhang, *Adv. Funct. Mater.* **2018**, *28*, 1703808; h) W. Zheng, J. Halim, A. El Ghazaly, A. S. Etman, E. N. Tseng, P. O. Å Persson, J. Rosen, M. W. Barsoum, *Adv. Sci.* **2021**, *8*, 2003656; i) W. Zheng, J. Halim, A. S. Etman, A. E. Ghazaly, J. Rosen, M. W. Barsoum, *Electrochim. Acta* **2021**, *370*, 137665; j) Z. Fan, Y. Wang, Z. Xie, X. Xu, Y. Yuan, Z. Cheng, Y. Liu, *Nanoscale* **2018**, *10*, 9642–9652; k) Y. Wang, X. Wang, X. Li, R. Liu, Y. Bai, H. Xiao, Y. Liu, G. Yuan, *Nano-Micro Lett.* **2020**, *12*, 115; l) Y. Tang, J. Zhu, W. Wu, C. Yang, W. Lv, F. Wang, *J. Electrochem. Soc.* **2017**, *164*, A923–A929; m) Y. Tian, C. Yang, W. Que, X. Liu, X. Yin, L. B. Kong, *J. Power Sources* **2017**, *359*, 332–339; n) X. Zhang, X. Liu, S. Dong, J. Yang, Y. Liu, *Appl. Mater. Res.* **2019**, *16*, 315–321.

Manuscript received: March 30, 2022

Revised manuscript received: May 20, 2022

Accepted manuscript online: May 21, 2022